ELSEVIER

Journal of Power Sources 109 (2002) 148–159

JOURNAL OF POWER SOURCES

www.elsevier.com/locate/jpowsour

A generalized model of the flow distribution in channel networks of planar fuel cells

Robert J. Kee*, Pavan Korada, Kevin Walters, Mark Pavol

Division of Engineering, Colorado School of Mines, Golden, CO 80401-1887, USA

Received 24 December 2001; accepted 18 January 2002

Abstract

A computational model is developed to describe the fluid flow in the small channel network systems that are typical of planar fuel cells. The model solves mass and momentum equations to predict pressure drop and flow uniformity within individual channels. By formulating the problem in dimensionless variables, the solutions are generalized in terms of two nondimensional groups. The results are presented in graphical form, facilitating their application without the need to solve the model for any particular application.

Keywords: Fuel cell; Model; Channel network

1. Introduction

Fuel cells are emerging as a practical technology for high-efficiency electric-energy generation. A planar architecture provides an effective approach, achieving high utilization of the electrochemically active area. Small channels, which are often formed in the interconnect material, carry the fuel and air gas flow. A designer must decide how to configure a channel network, such that the appropriate flow rates and flow uniformity can be maintained across the surfaces of the membrane-electrode assembly (MEA). An important consideration is the net pressure drop, which should be as low as possible to reduce parasitic power needed to drive pumps or compressors.

There is a great deal of current research on fuel cells generally, especially considering new material systems and electrochemical performance of the MEA assembly. However, relatively little of the literature concentrates on the system-level layout of the layers and stacks. Iwata et al. [1] provides one of the best overall analyses of a planar solid-oxide fuel-cell (SOFC) system. Boersma and Sammes [2] describe a model to predict flow in fuel-cell channel networks. Their model is based on networks of hydraulic resistances. However, the results of the model are not generalized or reported. Therefore, to apply the approach, one needs either to write a program that implements the model or obtain the authors' software.

The objective of this paper is to assist the designer in making quantitative decisions for the various channel dimensions. The analysis is based on a computational model that solves mass- and momentum-conservation equations within the channel network. Formulating the model in a dimensionless framework enables a generalization of the results in terms of two dimensionless parameter groups. The nondimensional results are presented in graphical form, establishing practical guidelines for channel layout and sizing.

While the principal intent of this work is to assist the design of fuel-cell systems, it should be noted that other applications can benefit from the results. For example, plate-and-frame heat exchangers often have a header-channel configuration that is similar to a planar fuel-cell layer. In that case, the hot and cold fluid channels take the place of the fuel and air channels in the fuel cell.

1.1. Planar SOFC architecture

Fig. 1 illustrates the principal features of a planar SOFC architecture. The membrane-electrode assembly (MEA) layer is composed of an electrolyte that is sandwiched between electrodes. The MEA layer is typically on the order of 1 mm thick, the details varying from one design to another. The electrodes (anode and cathode) are porous cermet materials that permit gases to be transported between

* Corresponding author. Tel.: +1-303-273-3379; fax: +1-303-273-3602.
E-mail address: rjkee@mines.edu (R.J. Kee).

0378-7753/02/$ – see front matter
PII: S0378-7753(02)00090-3

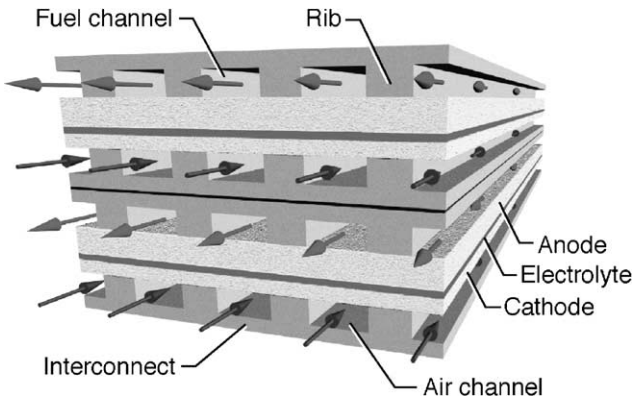

Fig. 1. Illustration of a segment of two fuel-cell layers, including the electrode-electrolyte assembly (MEA), the interconnect, and the flow channels for fuel and air. A counter-flow situation is illustrated here, but co-flow and cross-flow configurations are also common.

the flow channels and the electrolyte surface. The electrodes are loaded with a metal that serves two purposes. One is to catalyze electrochemical reaction at the electrode–electrolyte interfaces, and possibly to promote catalytic reaction of the fuel (e.g. reformation of hydrocarbon and water vapor to carbon monoxide and hydrogen). The other purpose of the electrode loading is to carry electric current from the electrolyte to the metal interconnect structure. As shown in Fig. 1, the flow channels are formed in the interconnect metal.

The ribs, which separate the flow channels, make direct contact with the electrodes. In designing the layer architecture, there is a tradeoff that must be considered between the rib and channel sizes. Thicker ribs may reduce the interface resistance to current flow by increasing the electrode-interconnect contact area and by decreasing the current path through the relatively high resistance electrode material. From a fluid-flow point of view, wide channels and narrow ribs facilitate more uniform distribution of reactive gases across the full area of the electrolyte and thus, promote electrochemical performance. The results of this paper assist the designer in understanding how channel sizing affects flow uniformity and pressure drops for the system.

A single MEA layer typically produces an areal power density that is on the order of 1 W/cm^2. Open circuit voltages are on the order of 1 V, with maximum power output at roughly 1/2 V. Maximum current densities are typically on the order of 5 A/cm^2. The performance of any particular system varies depending on a great many design and operational considerations. Because the layer voltage is less than 1 V, it is usually necessary to connect the layers in series to increase the voltage of a stack. As illustrated in Fig. 1, layers can be stacked one on top of another much as stacking batteries in a flashlight. To deliver a stack voltage of say 24 V, over 50 layers are needed. Thus, in addition to understanding flow distribution within a layer, one must also design to produce uniform flow to each layer in the stack.

1.2. Assumptions

The analysis here presumes an incompressible flow, i.e. the mass density ρ is constant. While the fluid is typically a gas (e.g. air or vaporized fuel), the flow velocities are quite low and the temperature is nearly uniform. Moreover, all other fluid properties (e.g. viscosity) are taken as constant. While incorporating variable properties presents no principle problems in the computational analysis, using constant properties facilitates a generalization of the results via characteristic nondimensional groups.

The following sections of this paper develop the governing equations and discuss their computational solution from the point of view of flow across a single fuel-cell layer. However, there is also a need to consider the flow through a stack, which is composed of many layers. Fortunately, the stack analysis follows directly from the layer analysis. For the stack analysis, the layer takes the role of the channels in the layer and the manifolds take the role of the headers.

The analysis here considers flow in impervious channels. It does not account for the mass flow through the electrolyte, and thus, the mass flow between the oxidizer and fuel channels. Certainly, this is a significant assumption for a fuel-cell application, the operation of which depends on the ion flux between the fuel and air channels. Nevertheless, the analysis represents a conservative limiting case for sizing the air channels (which lose mass in an SOFC cell). Because the air-flow rates are so large compared to the fuel flow, it is the air channels that typically demand the most design attention to achieve uniform flow. The intent of this analysis is to provide channel-sizing guidance in a generalized form. Incorporation of electrochemistry and the consequent mass exchange frustrates the ability to generalize the results, and thus, provide easy-to-use design guidance.

2. Governing equations

The flow distribution across a layer (e.g. Fig. 2) is based on solving mass-continuity and momentum equations along the length of the feed and exhaust headers. Fluid flows between the feed and exhaust headers via the channels that connect them. Thus, the conservation equations in the headers must accommodate the distributed mass loss from the feed header and the mass increase in the exhaust header.

It is clear from Fig. 2 that there are a certain number of channels in the layer and from Fig. 3 that there are a certain number of layers in the stack. With this, the system of equations are sensibly formulated and solved as a system of discrete algebraic equations that align with the channels or the layers. However, we find it beneficial to first derive the equations as systems of continuous differential equations. In a differential-equation form, it is easier to understand the mathematical structure and the requirements for boundary conditions. The solution, however, is accomplished in discrete form.

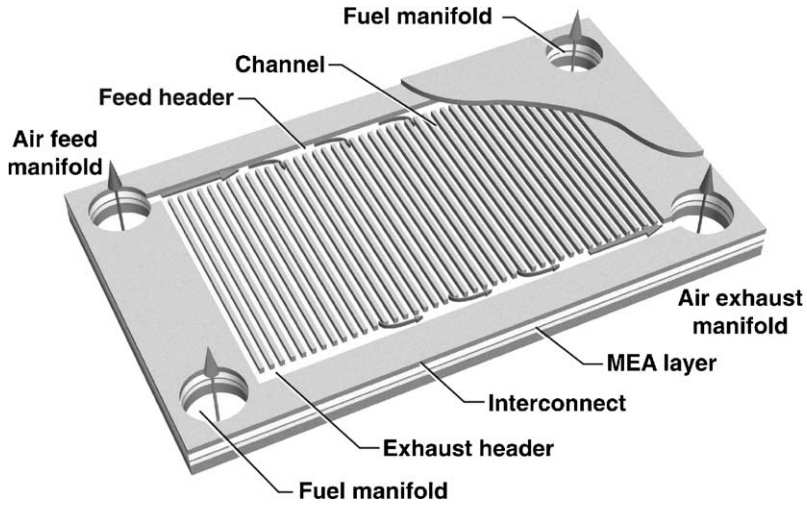

Fig. 2. Illustration of the flow distribution in a fuel-cell layer, showing the manifolds that carry flow between layers and the headers that distribute flow to the individual channels across the layer.

The analysis in the following sections concentrates on the layer. An analogy is then drawn between the layer and the stack, showing how the layer analysis is generalized to the stack.

2.1. Hagen–Poiseuille channel flow

For steady Hagen–Poiseuille flow in a channel, a net pressure variation is needed to balance the force caused by the shear stress at the walls

$$(p_f - p_e)A_c = \tau_w P_c L_c \tag{1}$$

where p_f and p_e represent pressures in the feed and exhaust headers, i.e. the inlet and outlet of a channel. Other variables are A_c, the channel cross-sectional area; P_c, the channel perimeter; and L_c, the length of the channel. The shear stress can be represented in terms of a nondimensional friction factor f as

$$f = \frac{\tau_w}{1/2\rho u^2} \tag{2}$$

where u is the mean velocity in the channel. For steady laminar flow in a channel, the product of the friction factor and the Reynolds number (based on mean velocity and a hydraulic diameter) is a constant,

$$\mathrm{Re}f = \text{constant} \tag{3}$$

where, for a circular channel $\mathrm{Re}f = 16$. The Reynolds number and the hydraulic diameter are written as

$$\mathrm{Re} = \frac{\rho u D_c}{\mu}, \quad D_c = \frac{4A_c}{P_c} \tag{4}$$

For rectangular channels, the value of $\mathrm{Re}f$ depends on the channel aspect ratio $\alpha = L/W$ as

$$\mathrm{Re}f \approx 13.74 + 10.38 \exp\left(\frac{-3.4}{\alpha}\right) \tag{5}$$

In a square channel $\mathrm{Re}f \approx 14$, while for a very high aspect-ratio channel $\mathrm{Re}f \approx 24$ [3].

Yuan, et al. [4] have simulated the flow in variously shaped fuel-cell channels. They report both $\mathrm{Re}f$ values as well as Nusselt numbers for heat-transfer analysis. In addition to studying channel shapes, they have also characterized the effects of mass transfer through the channel walls as happens in a fuel-cell channel. The results show that the mass transfer through the channel walls has a relatively small influence on the value of $\mathrm{Re}f$.

With a certain amount of algebra, an expression can be developed to relate the mass-flow rate in the channel to the net pressure difference from the channel inlet to the outlet

$$\dot{m}_c = \left(\frac{1}{\mathrm{Re}f}\frac{D_c^2 A_c}{2L_c}\frac{\rho}{\mu}\right)(p_f - p_e) = K_c(p_f - p_e) \tag{6}$$

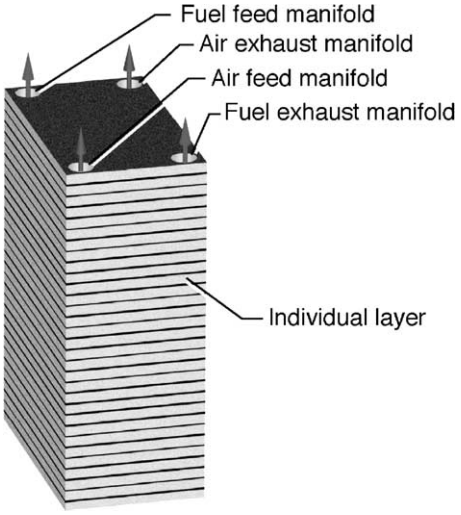

Fig. 3. Illustration of a full stack, with many individual layers. The fuel and air manifolds must feed each layer, and collect the exhaust from each layer.

where μ is the dynamic viscosity of the fluid. The constant K_c,

$$K_c = \frac{1}{\mathrm{Re}f}\frac{D_c^2 A_c}{2L_c}\frac{\rho}{\mu} \tag{7}$$

characterizes the proportionality between the mass-flow rate in a channel and the net pressure difference from inlet to outlet. In the fuel-cell layer, $p_f(z)$ and $p_e(z)$ are both functions of position in the header. Therefore, depending on the pressure distributions in the headers, the mass flow in each channel may be different.

In the foregoing analysis the flow conductance K_c is attributed to viscous effects in the channels. However, as discussed by Boersma and Sammes [2], other factors can contribute to flow resistance. These include expansion and contraction as the flow enters or leaves a channel or the resistance associated with the gas changing direction as it leaves the header and enters a channel. Imperfections or roughness in the channel walls can also increase flow resistance. All these effects can be incorporated into the present analysis by suitably reducing the value of K_c.

As noted earlier, the equations are first derived as continuous differential equations. Thus, it is necessary to represent the mass-flow rate between the headers as a continuous variable. The channel mass-flow rate per unit length of header (kg/m-s) may be written as

$$\dot{m}_c' = \frac{\dot{m}_c}{A_c'} = \frac{K_c(p_f - p_e)}{A_c'} = K_c'(p_f - p_e) \tag{8}$$

where A_c' is the channel-opening cross-sectional area per unit length of the header. In a limiting case, one can imagine an infinite number of channels, such that the flow between the feed and exhaust headers varies continuously along the length of the headers.

2.2. Continuity equation in headers

Derivation of the continuity equation is formulated for a differential control volume within a header (Fig. 4). Beginning with the Reynolds Transport Theorem (relating a system to a control volume) and the general mass-conservation law for a system, the continuity equation is given as

$$\left(\frac{\mathrm{d}m}{\mathrm{d}t}\right)_{\mathrm{sys}} = \int_{\mathrm{CV}}\left(\frac{\partial\rho}{\partial t} + \nabla\cdot\rho\boldsymbol{V}\right)\mathrm{d}V = \pm\int_{\mathrm{CS}}\dot{m}_e''\mathrm{d}A \tag{9}$$

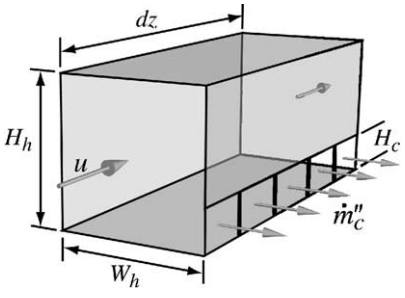

Fig. 4. Differential control volume for a section of a header.

where $\dot{m}_c''$ is the mass flux that leaves (or enters) the headers through the connecting channels. Note that the mass flow through the channels (i.e. between the headers) alters the system mass within the header control volume. For the constant cross-section headers, $\mathrm{d}V = A_h\mathrm{d}z$, where A_h is the cross-sectional area of the header (for a rectangular channel $A_h = H_h W_h$).

The area through which the channel flow leaves (normal to the header) is $\mathrm{d}A = A_c'\mathrm{d}z$. As illustrated for the rectangular channels in Fig. 4, $A_c' = H_c$. Shrinking the control volume to a differential length δz, the integrands can be considered as constants. Dividing by $\delta V = A_h\delta z$ and restricting attention to steady-state, one-dimensional flow provides the desired continuity equation in differential-equation form

$$\frac{\mathrm{d}(\rho u)}{\mathrm{d}z} = \pm\frac{A_c'}{A_h}\dot{m}_c'' \tag{10}$$

Assuming incompressible flow (i.e. ρ is constant),

$$\frac{\mathrm{d}u}{\mathrm{d}z} = \pm\frac{A_c'}{\rho A_h}\dot{m}_c'' = \pm\frac{\dot{m}_c'}{\rho A_h} \tag{11}$$

Substituting Eq. (8), the continuity equations take the form

$$\frac{\mathrm{d}u_h}{\mathrm{d}z} = \pm\frac{K_c'(p_f - p_e)}{\rho A_h} \tag{12}$$

where the subscript h = f refers to the feed header (right hand side takes the minus sign) and h = e refers to the exhaust header (right hand side is positive).

2.3. Momentum equation in headers

In general, the momentum balance is stated as

$$\left(\frac{\mathrm{d}\boldsymbol{P}}{\mathrm{d}t}\right)_{\mathrm{sys}} = \sum\boldsymbol{F} \tag{13}$$

where the extensive variable is the momentum vector $\boldsymbol{P} = m\boldsymbol{V}$ and $\boldsymbol{F}$ is a force exerted on the system. The intensive variable associated with the momentum is the velocity vector $\boldsymbol{V}$. Thus, for one-dimensional axial flow in the headers, the Reynolds Transport Theorem provides

$$\int_{\mathrm{CV}}\left(\frac{\partial\rho u}{\partial t} + \frac{\partial(\rho uu)}{\partial z}\right)\mathrm{d}V = \sum F_z \tag{14}$$

There are two forces that need to be considered. One is due to the pressure acting on the cross-sectional flow area and the other comes from viscous drag at the channel walls. Restricting attention to steady flow,

$$\int_{\mathrm{CV}}\frac{\partial(\rho uu)}{\partial z}\mathrm{d}V = \int_{\mathrm{CS}}\boldsymbol{\tau}_z\cdot\boldsymbol{n}\mathrm{d}A - \int_{\mathrm{CS}}\tau_w\mathrm{d}A \tag{15}$$

The first integral on the right-hand side represents the force due to normal stress on the control-volume faces in the flow direction. In this case, the normal stress is due entirely to the pressure, $\tau_z = -p$. The second integral represents the shear drag at the channel walls. The Gauss Divergence Theorem

can be used to convert the first integral on the right-hand side to a volume integral. The second integral is rewritten in terms of the differential length dz.

$$\int_{\mathrm{CV}} \frac{\partial(\rho u u)}{\partial z}\mathrm{d}V = \int_{\mathrm{CV}} \boldsymbol{\nabla}\cdot\boldsymbol{\tau}_z \mathrm{d}V - \int_z \tau_{\mathrm{w}} P_{\mathrm{h}} \mathrm{d}z \tag{16}$$

where P_{h} is the perimeter of the header channel (for the rectangular channel in Fig. 4, $P_{\mathrm{h}} = 2H_{\mathrm{h}} + 2W_{\mathrm{h}}$). Shrinking the control volume to vanishingly small δz, yields the desired differential equation as

$$\frac{\mathrm{d}(\rho u u)}{\mathrm{d}z} = -\frac{\mathrm{d}p}{\mathrm{d}z} - \frac{P_{\mathrm{h}}}{A_{\mathrm{h}}}\tau_{\mathrm{w}} \tag{17}$$

For an incompressible flow, the equation can be rewritten as

$$2\rho u \frac{\mathrm{d}u}{\mathrm{d}z} + \frac{\mathrm{d}p}{\mathrm{d}z} + \frac{P_{\mathrm{h}}}{A_{\mathrm{h}}}\tau_{\mathrm{w}} = 0 \tag{18}$$

As in the channel flow, the wall shear stress τ_{w} is determined in terms of a friction factor f, which depends on the header dimensions and fluid properties.

By substituting the expression for shear stress, the momentum equation can be rewritten as

$$2\rho u_{\mathrm{h}} \frac{\mathrm{d}u_{\mathrm{h}}}{\mathrm{d}z} + \frac{\mathrm{d}p_{\mathrm{h}}}{\mathrm{d}z} + \left(\frac{P_{\mathrm{h}}}{2A_{\mathrm{h}}D_{\mathrm{h}}}\mu \mathrm{Re} f\right) u_{\mathrm{h}} = 0 \tag{19}$$

Assuming constant properties is seen that the shear-stress term is the product of a constant factor and the local velocity. For the sake of simplifying the nomenclature, the constant in the shear-stress term may be defined as

$$F_{\mathrm{h}} = \frac{P_{\mathrm{h}}}{2A_{\mathrm{h}}D_{\mathrm{h}}}\mu \mathrm{Re} f \tag{20}$$

As in the continuity equation, a subscript h has been introduced to represent either the feed or the exhaust header. In the subsequent analysis, it is presumed that the feed and exhaust headers have the same dimensions, hence the same F_{h}.

2.4. Equation summary

In total, a system of four, coupled, nonlinear, first-order, ordinary differential equations describe the header flow

$$\frac{\mathrm{d}u_{\mathrm{f}}}{\mathrm{d}z} = -\frac{K'_{\mathrm{c}}(p_{\mathrm{f}} - p_{\mathrm{e}})}{\rho A_{\mathrm{h}}} \tag{21}$$

$$\frac{\mathrm{d}u_{\mathrm{e}}}{\mathrm{d}z} = +\frac{K'_{\mathrm{c}}(p_{\mathrm{f}} - p_{\mathrm{e}})}{\rho A_{\mathrm{h}}} \tag{22}$$

$$2\rho u_{\mathrm{f}} \frac{\mathrm{d}u_{\mathrm{f}}}{\mathrm{d}z} = -\frac{\mathrm{d}p_{\mathrm{f}}}{\mathrm{d}z} - \left(\frac{P_{\mathrm{h}}}{2A_{\mathrm{h}}D_{\mathrm{h}}}\mu \mathrm{Re} f\right) u_{\mathrm{f}} \tag{23}$$

$$2\rho u_{\mathrm{e}} \frac{\mathrm{d}u_{\mathrm{e}}}{\mathrm{d}z} = -\frac{\mathrm{d}p_{\mathrm{e}}}{\mathrm{d}z} - \left(\frac{P_{\mathrm{h}}}{2A_{\mathrm{h}}D_{\mathrm{h}}}\mu \mathrm{Re} f\right) u_{\mathrm{e}} \tag{24}$$

As illustrated in Fig. 5 for a layer, the independent-variable domain spans $0 \le z \le L_{\mathrm{h}}$.

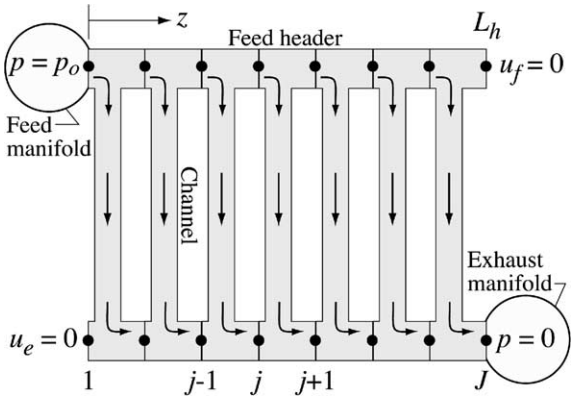

Fig. 5. Projection view of the header and channel layout, showing the unit cells of the finite-volume mesh network. In this illustration the headers are divided into seven unit cells, with eight mesh points. The boundary conditions are shown at the ends of the headers.

2.5. Boundary conditions

Since all the equations are first-order ordinary differential equations, each demands one boundary condition. Thus, in total, four boundary conditions are required. As indicated in Fig. 5, the velocity must be zero at the closed ends of the headers

$$u_{\mathrm{f}}(L_{\mathrm{h}}) = 0, \quad u_{\mathrm{e}}(0) = 0 \tag{25}$$

The pressures in the feed and exhaust manifolds can also provide suitable boundary conditions.

$$p_{\mathrm{f}}(0) = p_0, \quad p_{\mathrm{e}}(L_{\mathrm{h}}) = 0 \tag{26}$$

The exhaust-manifold pressure may be taken as a reference pressure of zero. However, for the application here, it is appropriate to specify the net mass-flow rate $\dot{M}_{\mathrm{l}}$ for the layer instead of the pressure in the feed manifold. Therefore, the feed pressure becomes an *implicit* boundary condition that must be determined during the course of the solution.

3. Nondimensionalization

With the objective of generalizing the results, the equations can be recast in terms of nondimensional variables. The reference length scale is the header-channel length L_{h} and the reference velocity is derived from the layer mass-flow rate $\dot{M}_{\mathrm{l}}$ as

$$U_{\mathrm{l}} = \frac{\dot{M}_{\mathrm{l}}}{\rho A_{\mathrm{h}}} \tag{27}$$

The reference velocity is the mean velocity that enters the feed header and exits the exhaust header. The reference pressure is a dynamic pressure based on the reference velocity

$$p_{\mathrm{ref}} = \rho U_{\mathrm{l}}^2 = \frac{\dot{M}_{\mathrm{l}}^2}{\rho A_{\mathrm{h}}^2} \tag{28}$$

The nondimensional variables are thus defined as

$$\hat{z} = \frac{z}{L_h}, \quad \hat{u} = \frac{u}{U_l} = \frac{\rho A_h}{\dot{M}_l} u, \quad \hat{p} = \frac{p}{p_{ref}} = \frac{p}{\rho U_l^2} = \frac{\rho A_h^2}{\dot{M}_l^2} p \tag{29}$$

Transformation of the continuity equations yields a nondimensional form as

$$\frac{d\hat{u}_h}{d\hat{z}} = \pm \frac{K_c' \dot{M}_l L_h}{\rho A_h^2} (\hat{p}_f - \hat{p}_e) = \pm \Omega_l' (\hat{p}_f - \hat{p}_e) \tag{30}$$

where the nondimensional group is defined as

$$\Omega_l' = \frac{K_c' \dot{M}_l L_h}{\rho A_h^2} \tag{31}$$

Transformation of the momentum equations leads to the following nondimensional form

$$2\hat{u}_h \frac{d\hat{u}_h}{d\hat{z}} + \frac{d\hat{p}_h}{d\hat{z}} + \frac{F_h L_h A_h}{\dot{M}_l} \hat{u}_h = 2\hat{u}_h \frac{d\hat{u}_h}{d\hat{z}} + \frac{d\hat{p}_h}{d\hat{z}} + \Gamma_l \hat{u}_h = 0 \tag{32}$$

Here, the nondimensional group is

$$\Gamma_l = \frac{F_h L_h A_h}{\dot{M}_l} = \left(\frac{P_h}{2D_h} \mu \mathrm{Re} f \right) \frac{L_h}{\dot{M}_l} \tag{33}$$

The Hagen–Poiseuille flow in the channels provided a relationship between the channel mass-flow rate and the pressure drop (Eq. (6)). Upon nondimensionalization,

$$\hat{\dot{m}}_c = \frac{\dot{m}_c}{\dot{M}_l} = \Omega_l (\hat{p}_f - \hat{p}_e) \tag{34}$$

The nondimensional mass-flow rate in an individual channel (normalized by the mass flow rate for the entire layer) is proportional to the nondimensional pressure drop for the channel. The nondimensional parameter is

$$\Omega_l = \frac{K_c \dot{M}_l}{\rho A_h^2} \tag{35}$$

The relationship between the continuous and discrete parameters is

$$\Omega_l = \frac{K_c}{K_c' L_h} \Omega_l' \tag{36}$$

4. Manifold-layer analysis

The foregoing analysis was presented from the point of view of a single layer. A fuel-cell stack is composed of many layers, with manifolds supplying and exhausting gas from the layers. Fortunately, there is an analogous analysis for the stack of layers. At the layer level, the individual channel flow is characterized by the factor K_c that was derived from Hagen–Poiseuille flow to relate the channel mass-flow rate to the pressure variation through the channel (Eq. (6)). At the stack level, an analogous K_l must be determined that relates the mass-flow rate through an individual layer $\dot{M}_l$ to the pressure difference between the feed manifold and the exhaust manifold $p_{m,f} - p_{m,e}$ at that layer.

The value of K_l follows from the solution of the layer problem. By definition of K_l

$$\dot{M}_l = K_l (p_f(0) - 0) \tag{37}$$

Since it is assumed that the exhaust pressure leaving the layer is at a reference value of zero (See Fig. 5), only the feed pressure appears in the above equation. Upon nondimensionalization,

$$\hat{\dot{M}}_l = \frac{\dot{M}_l}{K_l \rho U_l^2} = \frac{\rho A_h^2}{K_l \dot{M}_l} = \hat{p}_f(0) \tag{38}$$

The value of $\hat{p}_f(0)$ is determined from the solution of the nondimensional layer problem. Using the definition of Ω_l, it follows that

$$K_l = \frac{\rho A_h^2}{\hat{p}_f(0) \dot{M}_l} = \frac{K_c}{\hat{p}_f(0) \Omega_l} \tag{39}$$

Therefore, the value of K_l for the layer can be determined from the nondimensional solution for the layer.

With the value of K_l in hand, the analysis for the stack follows directly in the same form as the layer analysis. The two characteristic nondimensional numbers follow from the stack mass-flow rate and the manifold dimensions,

$$\Omega_s = \frac{K_l \dot{M}_s}{\rho A_m^2}, \quad \Gamma_s = \frac{F_m L_m A_m}{\dot{M}_s} = \left(\frac{P_m}{2D_m} \mu \mathrm{Re} f \right) \frac{L_m}{\dot{M}_s} \tag{40}$$

In these definitions, and throughout the analysis, the subscript l for the layer replaces the subscript c for the channel. Similarly, the subscript m for the manifold replaces the subscript h for the header. Of course, there generally are a different number of layers in the stack N_s than there are channels in the layer N_c.

5. Discretization

Because there are a discrete number of channels that connect the feed header to the exhaust header, it is appropriate to represent and solve the conservation equations in discrete form. Fig. 6 shows a header control volume, which forms the structure for the discrete continuity and momentum equations. For the purposes of illustration, the headers are taken as rectangular, with height and width H_h and W_h. Likewise, the connecting channels are rectangular, with dimensions H_c and W_c. The pitch S is the distance between channels (in the stack analysis, the pitch is the net thickness of a layer).

There are N_c discrete channels in the layer. Consequently, the headers may be discretized on a mesh of J nodes (Fig. 5), where the number of nodes is one greater than the number of channels, $J = N_c + 1$. Node $j = 1$ corresponds to the left boundary ($z = 0$) and $j = J$ corresponds to the right boundary

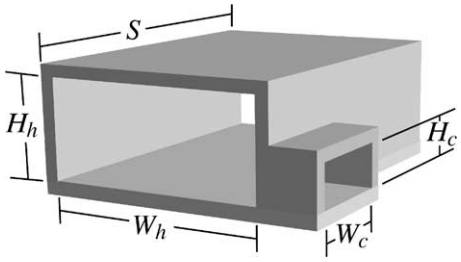

Fig. 6. Illustration of a control volume within a rectangular header, showing the entrance to a rectangular channel connecting the feed header to the exhaust header.

($j = J$). With the mesh aligned with the channels, it is evident that the mesh spacing is equal to the channel pitch, $\Delta z = S$.

As written in Eqs. (8) and (12), definition of $\dot{m}'_c$ and the continuity equation are written as though the mass-flow rate between the headers varies continuously with the position in the headers z and is proportional to the pressure difference between the headers. Accordingly, the proportionality constant K'_c that relates the mass-flow rate to the pressure difference is written on a per-unit-length basis. That is, K'_c has the units (kg-m/s-N). However, the individual channels are spaced along the headers with a pitch S (Fig. 6). Therefore, within each discrete control volume (Fig. 5) the mass-flow rate between the headers is determined from the Hagen–Poiseuille flow (Section 2.1). The relationship between the K'_c and K_c is $K_c = K'_c S$. In the nondimensional form, it follows that the nondimensional group in the continuity equation may be written as

$$\Omega'_1 = \frac{K_c \dot{M}_1 L_h}{\rho A_h^2 S} = \frac{K_c \dot{M}_1}{\rho A_h^2} N_c = \Omega_1 N_c \tag{41}$$

Note that the number of channels and the nondimensional mesh interval are related simply as

$$N_c = \frac{L_h}{S} = \frac{1}{\Delta\hat{z}} \tag{42}$$

Since the differential equations are first-order and because boundary conditions must be satisfied at each end of the header domain, it is appropriate to forward difference one of the equations and backward difference the other. In this way, one of the equations propagates boundary-condition information into the interior from each boundary. Even though the equations are coupled and must be viewed as a system, it can be helpful to notionally associate the continuity equation with velocity as its dependent variable and the momentum equation with pressure as its dependent variable. With this association in mind, it is reasonable to difference the continuity equation from the closed header ends and the momentum equation from the open manifold ends. Specifically, for the feed header,

$$\frac{\hat{u}_{f_{j+1}} - \hat{u}_{f_j}}{\Delta\hat{z}} = -\frac{\Omega_1(\hat{p}_{f_j} - \hat{p}_{e_j})}{\Delta\hat{z}} = -N_c\Omega_1(\hat{p}_{f_j} - \hat{p}_{e_j}), \quad (1 \le j \le J-1) \tag{43}$$

$$2\hat{u}_{f_j}\left(\frac{\hat{u}_{f_j} - \hat{u}_{f_{j-1}}}{\Delta\hat{z}}\right) + \left(\frac{\hat{p}_{f_j} - \hat{p}_{f_{j-1}}}{\Delta\hat{z}}\right) + \Gamma_1\hat{u}_{f_j} = 0, \quad (2 \le j \le J) \tag{44}$$

Note that the convective term in the momentum equation must respect an upwind difference. Presuming that the velocity is positive (i.e. in the direction of positive $\hat{z}$), the velocity derivative must be differenced so as to communicate information only in the flow direction. Failing to observe the upwind differencing leads to numerical instability.

In the exhaust header, the sense of the differencing is largely opposite that of the feed header,

$$\frac{\hat{u}_{e_j} - \hat{u}_{e_{j-1}}}{\Delta\hat{z}} = +\frac{\Omega_1(\hat{p}_{f_j} - \hat{p}_{e_j})}{\Delta\hat{z}} = N_c\Omega_1(\hat{p}_{f_j} - \hat{p}_{e_j}), \quad (2 \le j \le J) \tag{45}$$

$$2\hat{u}_{e_j}\left(\frac{\hat{u}_{e_j} - \hat{u}_{e_{j-1}}}{\Delta\hat{z}}\right) + \left(\frac{\hat{p}_{e_{j+1}} - \hat{p}_{e_j}}{\Delta\hat{z}}\right) + \Gamma_l\hat{u}_{e_j} = 0, \quad (1 \le j \le J-1) \tag{46}$$

Since the velocity is also positive in the exhaust header, the upwind differencing of the convective terms remains the same as in the feed header.

From the discrete form of the continuity equations (Eqs. (43) and (45)) it is apparent that the product $N_c\Omega_1$ can serve as the characteristic parameter instead of Ω_1 alone. Indeed, the solutions presented in subsequent sections are characterized in terms of $N_c\Omega_1$, making the nondimensional results applicable for any number of channels.

5.1. Boundary conditions

The nondimensional boundary conditions for velocity in the discrete system are stated as

$$\hat{u}_{f,J} = 0, \quad \hat{u}_{e,1} = 0 \tag{47}$$

At the end of the exhaust header, the pressure boundary condition is

$$\hat{p}_{e,J} = 0 \tag{48}$$

The final boundary condition is an implicit one in which the net mass-flow rate for the layer $\dot{M}_1$ is specified. The natural boundary condition $p_{f,1}$ must be determined in the course of the solution procedure (discussed in Section 6).

6. Numerical algorithm

The system of governing equations represents a boundary-value problem. Following discretization, the solution is accomplished by solving a system of nonlinear algebraic equations. The solution method used here is based on a modified Newton algorithm [5] and is implemented in the TWOPNT software [6].

The dependent variable vector $\boldsymbol{\phi}$ is comprised of the velocities and pressures at each of the mesh points in both of the headers. Thus, at each mesh point there are four dependent variables ($1 \le k \le 4$). In addition, the pressure in the feed manifold $\hat{p}_0$ represents a single dependent variable.

$$\boldsymbol{\phi} = (\hat{p}_0, \hat{u}_{\mathrm{f}_1}, \hat{p}_{\mathrm{f}_1}, \hat{u}_{\mathrm{e}_1}, \hat{p}_{\mathrm{e}_1}, \ldots, \hat{u}_{\mathrm{f}_j}, \hat{p}_{\mathrm{f}_j}, \hat{u}_{\mathrm{e}_j}, \hat{p}_{\mathrm{e}_j}, \ldots, \hat{u}_{\mathrm{f}_J}, \hat{p}_{\mathrm{f}_J}, \hat{u}_{\mathrm{e}_J}, \hat{p}_{\mathrm{e}_J})^T \tag{49}$$

To form a closed system of algebraic equations, there must be a corresponding set of four residual equations at each of the mesh points. That is, there is a vector of residuals $\boldsymbol{R}$ that is formed from the discrete form of the governing equations and boundary conditions. The length of $\boldsymbol{R}$ is $4N_\mathrm{c} + 1$.

A solution vector is sought for the solution vector that causes the residual vector to vanish, i.e.

$$\boldsymbol{R}(\boldsymbol{\phi}) = 0 \tag{50}$$

The Newton iteration for solving Eq. (50) may be written as

$$J(\boldsymbol{\phi}^{(m)})(\boldsymbol{\phi}^{(m+1)} - \boldsymbol{\phi}^{(m)}) = -\boldsymbol{R}(\boldsymbol{\phi}^{(m)}) \quad (m = 0, 1, 2, 3, \ldots) \tag{51}$$

where the Jacobian matrix

$$J(\boldsymbol{\phi}^{(m)}) = \frac{\partial \boldsymbol{R}}{\partial \boldsymbol{\phi}} \tag{52}$$

is evaluated at the (m)th iteration. The procedure begins with a "guess" at the solution vector $\boldsymbol{\phi}^{(0)}$. After solving the system of linear equations (Eq. (51)) for the "correction vector" $\Delta\boldsymbol{\phi}^{(m)} = (\boldsymbol{\phi}^{(m+1)} - \boldsymbol{\phi}^{(m)})$, the $(m+1)$th iteration to the solution is given as

$$\boldsymbol{\phi}^{(m+1)} = \boldsymbol{\phi}^{(m)} + \Delta\boldsymbol{\phi}^{(m)} \tag{53}$$

The iteration procedure continues until the correction becomes negligibly small. Insofar as the initial iterate lies within a domain of convergence, Newton's method converges very rapidly (quadratically). For the problem at hand, the Newton algorithm is quite robust. At each mesh point, including the boundaries, the discrete equations may be written in a residual form. For example, the residuals of the continuity equation in the feed header ($k = 1$) may be written as

$$\begin{aligned} R_{1,j} &= \frac{\hat{u}_{\mathrm{f}_{j+1}} - \hat{u}_{\mathrm{f}_j}}{\Delta\hat{z}} + N_\mathrm{c}\Omega_1(\hat{p}_{\mathrm{f}_j} - \hat{p}_{\mathrm{e}_j}), \quad (1 \le j \le J-1) \\ R_{1,j} &= 0 - \hat{u}_{\mathrm{f}_j}, \qquad (j = J) \end{aligned} \tag{54}$$

Similarly, the feed–header momentum equation ($k = 2$) is written as

$$\begin{aligned} R_{2,j} &= 2\hat{u}_{\mathrm{f}_j}\left(\frac{\hat{u}_{\mathrm{f}_j} - \hat{u}_{\mathrm{f}_{j-1}}}{\Delta\hat{z}}\right) + \left(\frac{\hat{p}_{\mathrm{f}_j} - \hat{p}_{\mathrm{f}_{j-1}}}{\Delta\hat{z}}\right) + \Gamma_1\hat{u}_{\mathrm{f}_j}, \quad (2 \le j \le J) \\ R_{2,j} &= p_0 - \hat{p}_{\mathrm{f}_j}, \qquad (j = 1) \end{aligned} \tag{55}$$

Finally, there is a residual equation that relates the velocity (from the feed manifold) into the feed header to the specified mass-flow rate for the layer. The residual equation is

$$R_1 = 1 - \hat{u}_{\mathrm{f},1} \tag{56}$$

By definition, the reference velocity U_1 is the mean velocity that enters the feed header from the manifold. Therefore, the manifold residual equation requires that $u_{\mathrm{f},1} = U_1$, or $\hat{u}_{\mathrm{f},1} = 1$. Note that the associated dependent variable (the first variable in the dependent variable vector) is the manifold pressure $\hat{p}_0$, not a velocity as might be expected. This is a so-called implicit boundary condition.

The TWOPNT boundary-value-problem software is designed especially to accommodate implicit constraints or boundary conditions such as represented by the first residual equation. It is also designed to take advantage of a Jacobian with a band structure such as in this problem.

7. Design space

To explore potential design space, the nondimensional problem is solved for essentially all plausible combinations of Γ_1 and $N_\mathrm{c}\Omega_1$. Fig. 7 is a nondimensional map that provides quantitative information about layer performance as a function of Γ_1 and $N_\mathrm{c}\Omega_1$. The flow-uniformity contours,

$$\frac{\Delta\hat{\dot{m}}_\mathrm{c}}{\hat{\dot{m}}_\mathrm{c}} = \frac{\max(\hat{\dot{m}}_\mathrm{c}) - \min(\hat{\dot{m}}_\mathrm{c})}{\max(\hat{\dot{m}}_\mathrm{c})} \tag{57}$$

represent the relative difference between the mass-flow rates in each of the N_c channels. Assuming that uniform flow is desired, a good layer design would result in a small value of $\Delta\hat{\dot{m}}_\mathrm{c}/\hat{\dot{m}}_\mathrm{c}$. The design space for $\Delta\hat{\dot{m}}_\mathrm{c}/\hat{\dot{m}}_\mathrm{c} < 0.1$ is visually apparent from Fig. 7 as the tent-shaped region below the

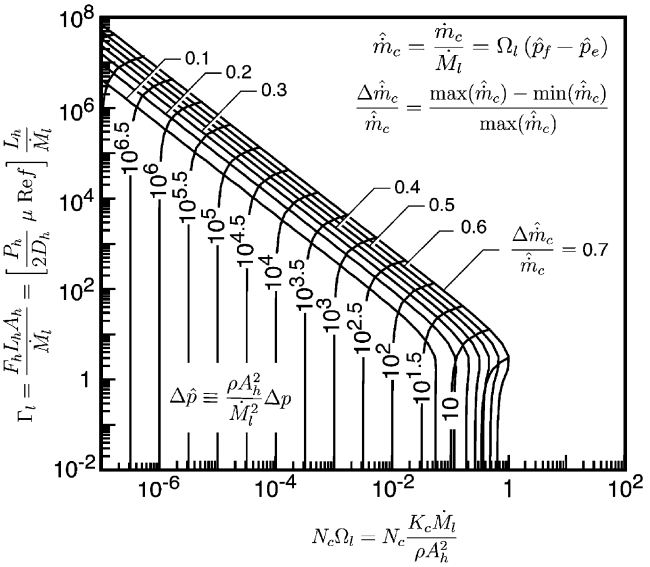

Fig. 7. Contours of the nondimensional pressure drop and channel-flow uniformity as a function of Γ_1 and $N_\mathrm{c}\Omega_1$.

10% uniformity contour. Quantitatively, this space is bounded by

$$N_c\Omega_l < 5 \times 10^{-2}, \quad \text{and} \quad 2.5\Gamma_l N_c\Omega_l < 1 \tag{58}$$

Within the uniform-flow region, the nondimensional pressure drop is seen to depend only on $N_c\Omega_l$ as

$$\Delta\hat{p} \equiv \frac{\rho A_h^2}{\dot{M}_l^2}\Delta p = \frac{1}{N_c\Omega_l} \tag{59}$$

In the region above and to the right of the uniformity contours, some channels have no flow, or, potentially, reverse flow. Therefore, because these regions are of no interest to applications like fuel cells they are not investigated.

7.1. Flow distribution

Fig. 8 illustrates how the flow distribution in individual channels varies for different combinations of Ω_l and Γ_l. The bar charts, which are evaluated for $N_c = 50$ channels, show the nondimensional mass flow in each channel. The inlet is on the left side and the outlet is on the right. By definition of the nondimensional mass flow rate (Eq. (34)),

$$\sum_{n=1}^{N_c} \hat{\dot{m}}_c = 1 \tag{60}$$

Thus, everywhere in the uniform-flow region, each of the 50 channels has a flow rate of $\hat{\dot{m}}_c = 2 \times 10^{-2}$.

The channel-flow distribution changes qualitatively in the different regions of nonuniform flow. For low values of $N_c\Omega_l$, where the uniformity contours appear as downward-sloping lines, the channel-flow distribution is symmetric with minimum flow in the center channels. For low values of Γ_l, where the uniformity contours appear as vertical lines, the channel-flow distribution increases monotonically from a minimum flow near the inlet to a maximum flow near the outlet. In the knee region where the uniformity contours turn the corner from sloping to vertical lines, the channel-flow distribution transitions from the center-low distribution to the monotonically increasing distribution.

It is apparent that the nondimensional pressure drop increases as $N_c\Omega_l$ decreases. At first, this trend may seem counterintuitive, since, for example, lower $N_c\Omega_l$ can result from lower channel conductance K_c or lower mass flow rate $\dot{M}_l$. However, note that the definition of the nondimensional pressure can be written to involve Ω_l as

$$\Delta p = \frac{\dot{M}_l^2}{\rho A_h^2}\Delta\hat{p} = \frac{\dot{M}_l}{K_c}\Omega_l\Delta\hat{p} \tag{61}$$

Thus, in the uniform-flow region, where $\Delta\hat{p} = 1/N_c\Omega_l$, an anticipated result is recovered,

$$\Delta p = \frac{\dot{M}_l}{K_c N_c} \tag{62}$$

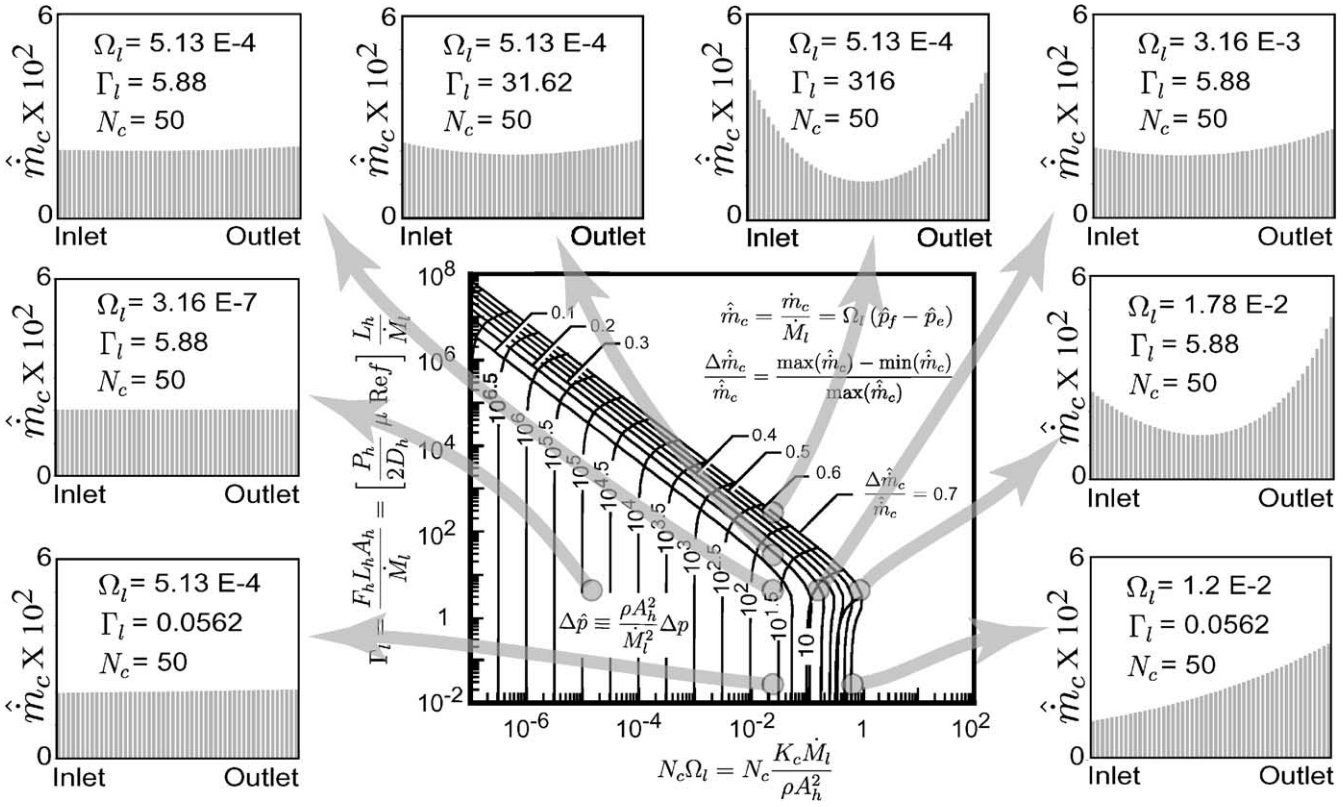

Fig. 8. Illustration of the channel-flow distributions as a function of Ω_l and Γ_l.

7.2. Mathematical analysis of the map

The qualitative behavior of the solutions can be understood from the structure of the differential equations. Restated, the continuity and momentum equations are

$$\frac{d\hat{u}_f}{d\hat{z}} = -\Omega_l'(\hat{p}_f - \hat{p}_e) \tag{63}$$

$$\frac{d\hat{u}_e}{d\hat{z}} = +\Omega_l'(\hat{p}_f - \hat{p}_e) \tag{64}$$

$$2\hat{u}_f \frac{d\hat{u}_f}{d\hat{z}} = -\frac{d\hat{p}_f}{d\hat{z}} - \Gamma_l \hat{u}_f \tag{65}$$

$$2\hat{u}_e \frac{d\hat{u}_e}{d\hat{z}} = -\frac{d\hat{p}_e}{d\hat{z}} - \Gamma_l \hat{u}_e \tag{66}$$

Were it not for the convective term in the momentum equations, the equations and boundary conditions preserve a certain symmetry. For example, the velocities in the channels would take the form $\hat{u}_e = 1 - \hat{u}_f$. The pressure difference between feed and exhaust channels would be symmetric about the center channel.

7.2.1. Large Γ_l

For sufficiently large values of Γ_l, the drag term in the momentum equation, $\Gamma_l \hat{u}$, dominates and the convective term becomes negligible. Under these circumstances the flow must be symmetric. As illustrated in Fig. 8, the nonuniform channel flow is always symmetric for $\Gamma_l > 10$. Fig. 9 illustrates in more detail the velocity and pressure profiles in the headers as well as the channel mass-flow rates for a symmetric, but nonuniform flow.

It may be observed that Ω_l and Γ_l are related through $\dot{M}_l$. Combining the two definitions by eliminating $\dot{M}_l$ yields

$$\Omega_l \Gamma_l = \frac{K_c F_h L_h}{\rho A_h^2} = \Psi_l \tag{67}$$

The new nondimensional group Ψ_l depends on the header and channel geometry and the fluid properties, but not the flow rates. Thus, for a fixed layer and channel layout, the product $\Omega_l \Gamma_l$ is a constant. Taking the logarithm of the equation yields

$$\log(\Gamma_l) = -\log(\Omega_l) + \log(\Psi_l) \tag{68}$$

which, on a log–log scale (as Fig. 7), is the equation of a straight line with a slope of negative unity. This observation is relevant in understanding the nondimensional mass flow-rate distribution along equi-uniformity contours.

Consider the governing equations in the high Γ_l region, where the convective term is negligible. After multiplying the momentum equation by Ω_l', the system becomes

$$\frac{d\hat{u}_h}{d\hat{z}} = \pm\Omega_l'(\hat{p}_f - \hat{p}_e) \tag{69}$$

$$\Omega_l' \frac{d\hat{p}_h}{d\hat{z}} + \Omega_l' \Gamma_l \hat{u}_h = \Omega_l' \frac{d\hat{p}_h}{d\hat{z}} + \Psi_l' \hat{u}_h = 0 \tag{70}$$

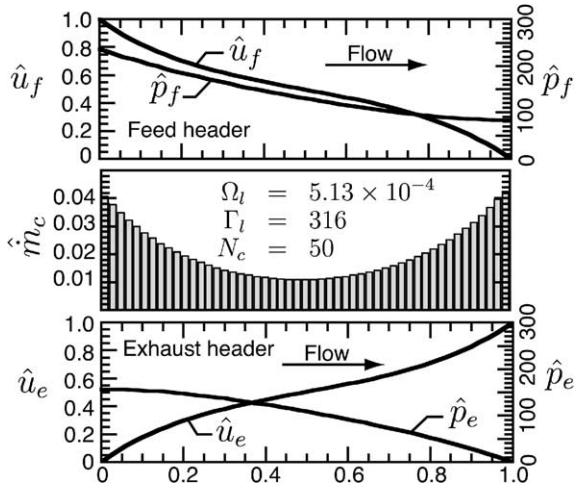

Fig. 9. Nondimensional velocity and pressure profiles in the feed and exhaust headers as well as the nondimensional mass-flow rate in each of 50 individual channels. At relatively high Γ_l, the flow is seen to be symmetric but not uniform.

In this form it is clear that the product $\Omega_l' \hat{p}$ depends only on the nondimensional parameter Ψ_l'. In the high Γ_l region, the uniformity contours on the log–log plot (Figs. 7 and 8) are a straight line with slope of negative unity. Therefore, along any uniformity contour, the product $\Omega_l \Gamma_l = \Psi_l$ is a constant. It follows that anywhere along a certain uniformity contour (in the high Γ_l region), the solutions within the headers must produce the same profiles of $\Omega_l \hat{p}(\hat{z})$. Furthermore, since the nondimensional mass-flow rates are

$$\hat{\dot{m}}_c = \Omega_l(\hat{p}_f - \hat{p}_e) \tag{71}$$

the nondimensional mass-flow rate distribution must be the same anywhere along a certain uniformity contour.

7.2.2. Small Γ_l

For sufficiently small values of Γ_l, the drag term in the momentum equation becomes negligible and the convective term dominates. Consequently, the nonuniform flow must be asymmetric. Furthermore, when the $\Gamma_l \hat{u}$ term is negligible, the solutions depend *only* on Ω_l. This behavior is seen easily in Fig. 7, where both the nondimensional pressure and uniformity contours are vertical lines. Fig. 10 illustrates solutions in the Γ_l-independent region and at high enough $N_c \Omega_l$ that the channel flow is significantly nonuniform.

7.2.3. Small Γ_l and $N_c \Omega_l$

The behavior for low values of both Ω_l and Γ_l can be seen by substituting the continuity equation into the momentum equation, yielding

$$\hat{u}_f[\Gamma_l - 2\Omega_l'(\hat{p}_f - \hat{p}_e)] + \frac{d\hat{p}_f}{d\hat{z}} = 0 \tag{72}$$

$$\hat{u}_e[\Gamma_l + 2\Omega_l'(\hat{p}_f - \hat{p}_e)] + \frac{d\hat{p}_e}{d\hat{z}} = 0 \tag{73}$$

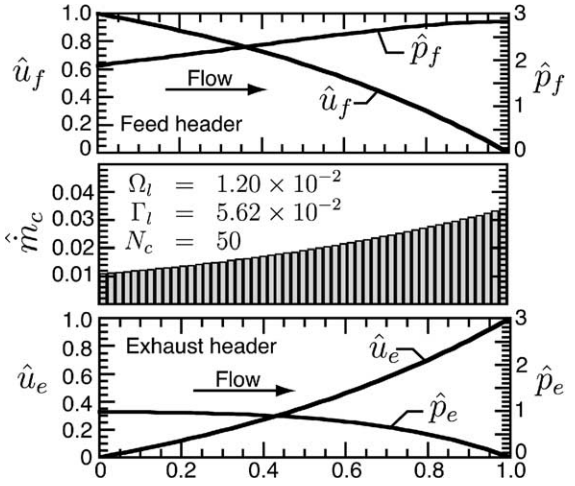

Fig. 10. Nondimensional velocity and pressure profiles in the feed and exhaust headers as well as the nondimensional mass-flow rate in each of 50 individual channels. At relatively low Γ_l and $N_c\Omega_l$ near unity, the flow is seen to be asymmetric and nonuniform.

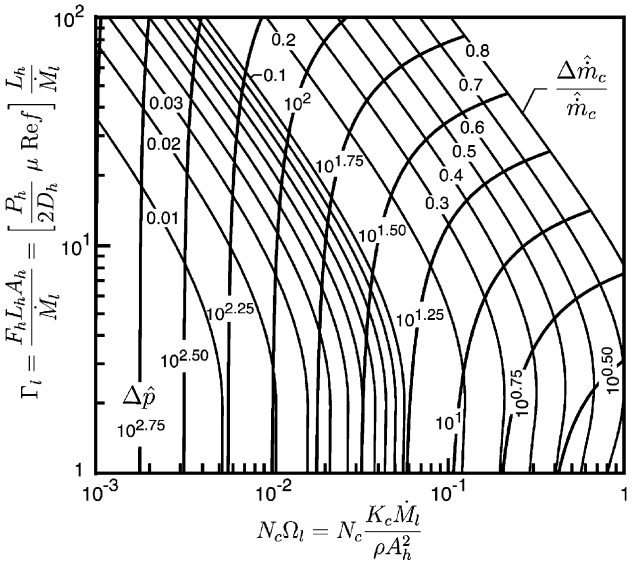

Fig. 12. Enlarged views of the nondimensional map in the region of the knee in the uniformity contours.

When both Ω_l and Γ_l are sufficiently small, the pressure gradients are very small and the pressure is nearly uniform in both the feed and exhaust headers. Thus, the channel flow is highly uniform.

7.2.4. Knee region

In the region around $\Gamma_l \approx 10$, where the drag and convective terms are comparable, the channel flow transitions from the symmetric to the asymmetric patterns. Fig. 11 illustrates a solution in the knee region, where both the convective and drag terms in the momentum equation are comparable.

As practical matter, the best design space tends to be near the inside of the knee of the uniformity contours, i.e. around $N_c\Omega_l \approx 10^{-2}$ and $\Gamma_l \approx 1$. Moving farther into the uniform region usually comes at the cost of large header cross-sections and low flow rates, or large pressure drops associated with small channel dimensions (i.e. small K_c). Thus, to use the active area of a fuel-cell layer to best advantage, a good compromise is to operate near the regions of nonuniformity with $N_c\Omega_l$ as high as possible. Fig. 12, which is an enlargement of the nondimensional map near the knee in uniformity contours, provides more detailed contours that facilitate quantitative analysis.

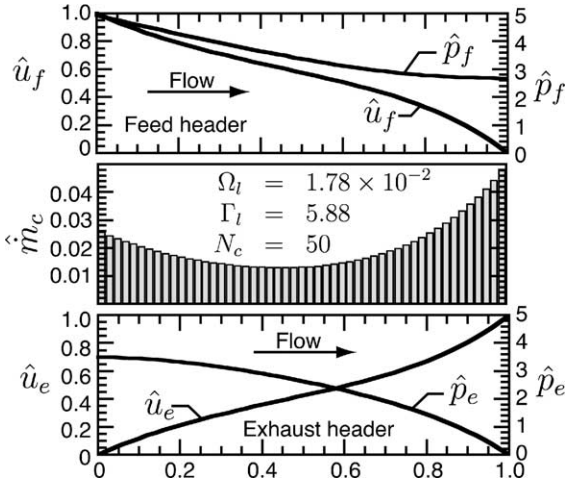

Fig. 11. Nondimensional velocity and pressure profiles in the feed and exhaust headers as well as the nondimensional mass-flow rate in each of 50 individual channels. This simulation is near the outside of the knee in the uniformity contours, where the flow is in transition between the symmetric and asymmetric behavior.

8. Channel variations

In fuel-cell applications, the channel dimensions can be very small (order millimeter). Furthermore, depending on manufacturing processes, the exact dimensions may be difficult to control and they can have imperfections such as in surface finishes. Consequently, it is interesting to know how such variations may affect flow characteristics.

Consider a situation in which the flow is nominally uniform, such as flow represented by the upper left-hand panel of Fig. 8. This flow represents a reasonable design, just inside the knee of the uniformity contours. To represent variations in channel characteristics, the value of Ω_l for each of 50 channels is varied randomly by $\pm 10\%$ about its nominal value. Fig. 13 illustrates the effect on channel flow distribution.

From Eq. (7), it is seen that the channel conductance K_c depends strongly on the channel-cross-section dimensions. Specifically, K_c depends on the cube of a characteristic channel dimension (e.g. its height). Therefore, a 10% variation in channel height causes a much larger variation in K_c, and consequently Ω_l. As a result, to assure uniform flow,

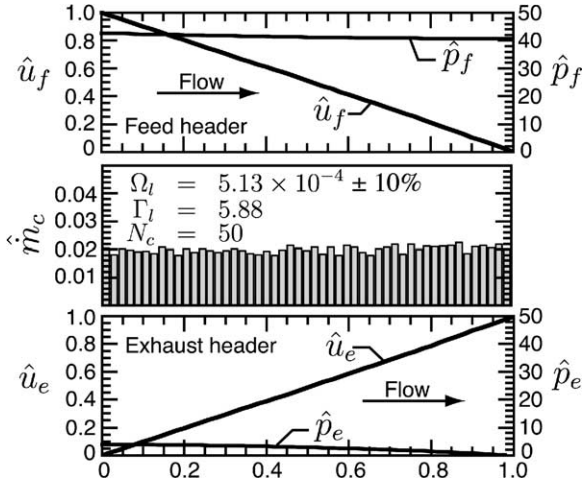

Fig. 13. Nondimensional velocity and pressure profiles in the feed and exhaust headers as well as the nondimensional mass-flow rate in each of 50 individual channels. This simulation is near the inside of the knee in the uniformity contours, where the flow is nearly uniform. To represent the effect of fabrication tolerances, the value of Ω_l is varied randomly by $\pm 10\%$ in each channel.

there is a very important demand on fabrication processes to maintain control of channel dimensions.

9. Conclusions

An analysis has been developed to characterize the flow distribution in planar fuel-cell layers and stacks. Using nondimensional variables, the results are presented in graphical form that can be applied generally. While the analysis is principally motivated by fuel-cell applications, other applications like plate-and-frame heat exchangers can benefit from the results.

Acknowledgements

This work was supported by the National Institute of Standards and Technology through the Advanced Technology Program, Co-operative Agreement Number 70NANBOH3025. We gratefully acknowledge the close collaborations with ITN Energy Systems in the development of fuel-cell applications.

References

[1] M. Iwata, T. Hikosaka, M. Morita, T. Iwanari, K. Ito, K. Onda, Y. Esaki, Y. Sakaki, S. Nagata, Performance analysis of planar-type unit SOFC considering current and temperature distributions, Solid State Ionics 132 (2000) 297–308.

[2] R.J. Boersma, N.M. Sammes, Computational analysis of the gas-flow distribution in solid oxide fuel cell stacks, J. Power Sources 63 (1996) 215–219.

[3] W.M. Kays, M.E. Crawford, Convective Heat and Mass Transfer, McGraw-Hill, New York, 1980.

[4] J. Yuan, M. Rokni, B. Sundén, Simulation of fully developed laminar heat and mass transfer in fuel cell ducts with different cross-sections, Intl. J. Heat Mass Transfer 44 (2001) 4047–4058.

[5] J.F. Grcar, R.J. Kee, M.D. Smooke, J.A. Miller, A hybrid Newton/time-integration procedure for the solution of steady, laminar, one-dimensional premixed flames, Proc. Combust. Inst., 21 (1986) 1773-1782.

[6] J.F. Grcar, The TWOPNT program for boundary value problems, Technical Report SAND91-8230, Sandia National Laboratories, 1992.